The Effect of Shape on the Motion and Stability of Marangoni Surfers

Samrat Sur
Department of Mechanical and Industrial
Engineering,
University of Massachusetts,
Amherst, MA 01003

Nicholas Uvanovic
Department of Mechanical and Industrial
Engineering,
University of Massachusetts,
Amherst, MA 01003

Hassan Masoud
Department of Mechanical Engineering-
Engineering Mechanics,
Michigan Technological University,
Houghton, MI 49931

Jonathan P. Rothstein
Department of Mechanical and Industrial
Engineering,
University of Massachusetts,
Amherst, MA 01003
e-mail: rothstein@ecs.umass.edu

The Marangoni propulsion of spheres and elliptical disks floating on the air–water interface were studied to understand the effect of particle shape on its motion and its stability at moderate Reynolds numbers. Self-propulsion of the Marangoni surfer was achieved by coating half of the spheres and the elliptical disks with either a solution of soap or isopropyl alcohol (IPA). The presence of the soap or IPA resulted in a surface tension gradient across the particles which propelled the particles in the direction of increasing surface tension. Beyond a critical velocity, a transition was observed from a straight-line motion to a rotational motion. These vortices were observed to shed above a critical Reynolds number resulting in an unbalanced torque that caused the particles to rotate. Increasing the aspect ratio between the major and minor axes of the elliptical disks was found to decrease their stability and greatly enhance their rate of rotation. This was especially true for elliptical disks traveling in a direction parallel to their major axis. The interactions between the particles and the wall of a Petri dish were also studied. Repulsive, concave curvature was found to decrease stability and enhance rotational motion, while attractive, convex curvature was shown to stabilize the straight-line motion of the spheres. For the neutrally buoyant elliptical disks, the presence of the bounding wall was found to greatly stabilize the straight-line motion of the elliptical disks when they were traveling in a direction parallel to their minor axis. [DOI: 10.1115/1.4048139]

1 Introduction

For small objects, insects or bacteria floating on a liquid interface, locomotion can be induced by localized manipulation of the chemical composition or temperature of the liquid interface to produce surface tension gradients [1]. The Marangoni flow that results typically propels the interfacial surfers in the direction of higher surface tension. Perhaps the most prominent examples of Marangoni surfers in the literature are the camphor boats that are commonly used for demonstration in the classroom [2–4]. Symmetric boat designs propelled by interfacial tension gradients tend to move with a purely translational motion and speeds that can be in excess of 10 cm/s. This is because, at low Reynolds numbers, rotational perturbation to the flow field damp out. As a result, symmetric surfers tend to follow a straight-line path [5]. In order to achieve rotational motion at low Reynolds numbers, asymmetries in the boat or particle design are needed [4,6]. The direction and strength of rotational motion has been shown to be primarily dictated by the shape of the particle and the asymmetry of release of the surface active chemicals [7,8]. With careful design, the rotation rate of the particles can be maximized [9,10] making the design of interfacial rotors possible.

Marangoni propulsion has been observed in biological organisms as small as bacteria and as large as water-walking insects. Many bacteria like *Pseudo-monas aeruginosa*, which tend to reside at the water interface, are known to use the excretion of biomolecules to reduce surface tension in order to induce a Marangoni flow and rapidly migrate toward nutrient-rich regions ripe for feeding and colonialization [11,12]. Water-walking insects like water striders rove beetles are also known to excrete surface-active fluids to induce a Marangoni flow in order to boost their locomotion speed during emergency escape situations [13–16]. The path taken by these water walking insects is initially straight, however, a deviation of the insect from a straight line trajectory is often observed after a short distance [16]. This rotational motion could be induced by insect using its legs like oars to steer or, as recently shown by Sur et al. [6], the observed rotational motion could be the result of vortex shedding that can occur at the moderate Reynolds numbers resulting from the Marangoni flow generated by the insect.

Sur et al. [6] have experimentally investigated the interfacial and bulk flow dynamics of circular disk-shaped Marangoni surfers propelled by a solution of soap or isopropyl alcohol (IPA) through particle image velocimetry (PIV) measurements and particle tracking. For the case of soap, the circular disk was found to follow a translational steady-state motion with a pair of attached counter-rotating vortices along the side of the circular disk. For this steady, straight line motion a maximum Reynolds number of no more than $Re = \rho U D/\mu = 60$ was reached. Here, ρ is the fluid density, U is the disk velocity, D is the disk diameter, and μ is the fluid viscosity. For the case of IPA, the driving force was larger and the corresponding circular disk and interfacial velocities were found to be much higher with Reynolds numbers greater than $Re > 600$. At these moderately high Reynolds numbers, inertial effects become significant and a transition from a straight-line motion to an orbital rotational motion was observed for any case were a peak Reynolds number of at least $Re = 180$ was achieved. From PIV investigation, it was found that the rotation of the circular disk was caused by vortex shedding. The shedding of an attached vortex provided a sufficiently large unbalanced torque to spin the circular disk and initiate its orbital motion. In this paper, our goal is to understand how the Marangoni surfer symmetry, shape, and orientation affects its motion and stability.

The Marangoni flow of particles attached to an interface has also been investigated both theoretically and through numerical computations, but only in the regime of vanishingly small Reynolds numbers where straight line translational motion is expected [17–22]. Masoud and Stone [19] derived a closed-from expression for the speed of propulsion of both chemically active oblate and prolate spheroids using the reciprocal theorem. To examine the collective motion of many particles attached to an interface, Masoud and Shelley [20] employed a Fourier spectral method. In a recent work, Vandadi et al. [21] used theory to examine the motion of particles in a Marangoni flow confined by a solid wall

---

located just below the air–water interface. Their calculations showed that the propulsion speed and direction of the particles depend both on the particle geometry and the degree of confinement introduced by the presence of the bottom wall. One remarkable finding of their work was that when the gap between the bottom of the floating particle and the bottom wall decreased below a critical threshold, hemispherical particles change direction, and begin to move toward the direction of lower surface tension. This reverse Marangoni flow was not observed for the flat disk-shaped particles in their study. The calculations of Vandadi et al. [21] show just how important the shape of particle above and below the water line can be. In this study, we experimentally investigate the effect that particle shape can have on the speed and stability of the Marangoni-induced motion of surfers at moderate Reynolds numbers by studying the dynamics of both spherical particles and elliptical disk-shaped particles with cross sections of various aspect ratios. By comparing the results to each other and to the cylindrical disk-shaped particles studied previously [6], the effect of particle shape, orientation, and symmetry will become clear.

In addition to shape variation of the particles, in this study, we investigate the importance of particle buoyancy and interface deformation on the stability of Marangoni surfers. Unlike the elliptical disks used here and the circular disks used previously [6], the air–water interface around the spherical particles is not flat. Due to its density and shape, the spheres floats with more than 50% of the sphere submerged below the water line. To maintain the correct contact angle on the sphere, the air–water interface is forced to curve and become convex. The surface tension along this curved interface helps to support the weight of the spheres. On a flat interface, the interfacial curvature around a single particle will not cause spontaneous particle motion. However, a second spherical particle on the interface or a boundary wall which also supports a convex interfacial curvature will result in an attractive capillary force [23] that increases with one over the separation distance between the two objects [24]. Objects with like (concave or convex) interfacial curvature attract each other because both the capillary and gravitational potential energy decrease with decreasing separation of the objects [24]. For small floating objects, these capillary forces can be quite strong and are known to result in the self-assembly of particle rafts [24–28] especially in regions of highest interfacial curvature [29,30]. The presence of curvatures at the boundary and its effect on the motion of the disks propelled by a Marangoni flow was investigated by Sur et al. [6]. In their experiments, the presence of a concave curvature at the boundary lead to rotational motion of circular disk-shaped particles at a Reynolds numbers much lower than what was observed on flat, unbounded interfaces. Conversely, flat and convex interface curvatures did not lead to additional destabilization of the unbounded translational motion of the disks. In the experiments presented in this paper, we will investigate how the particle shape, the particle orientation and the local curvature that exists around particle affect its dynamics and stability as it approaches a series of bounding walls with different interface curvatures.

2 Experimental Setup

A series of experiments were performed in both a large, $D_{dish} = 150$ mm, and a small, $D_{dish} = 86$ mm, Petri dish as shown in Fig. 1. The depth of water was set to be $h = 12$ mm and 70 mm in the small and large Petri dishes, respectively. In all cases, the
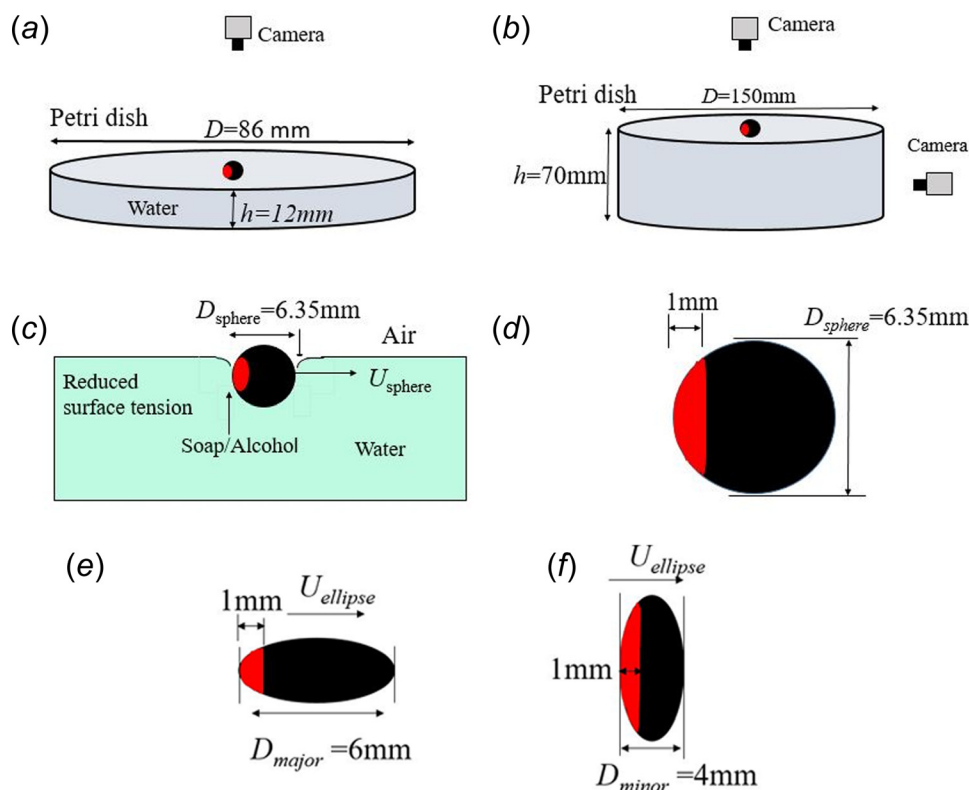

Fig. 1 Schematic diagram of the experiments performed in (a) the small Petri dish and (b) the large Petri dish. All necessary dimensions are given in the figure. Both a side and top mounted camera were used to record the motion of the particles as shown in (b). Both the sphere shown in (c) and (d) and the AR = 1.5 elliptical disk shown in (e) and (f) were propelled by a Marangoni flow induced by the release of soap or alcohol from a 1 mm strip shown in red which was applied to the back of the particle through a dip coating process. The elliptical disks were $t = 1.5$ mm thick.

depth of the water in the Petri dish was sufficient to eliminate all effects of confinement from the bottom surface of the Petri dish. The large Petri dish was used to avoid interaction between the Marangoni surfer with the sidewalls of the dish, while the small Petri dish used to explicitly study the effect that the interface curvature can have on the stability of the translational motion of the spherical and elliptical Marangoni surfers. In order to vary the strength of propulsion, solutions of a commercially available soap (Dawn) and IPA in water were used to generate the surface tension gradients responsible for inducing the Marangoni flow. Each $D = 6.35$ mm sphere and 6 mm $\times$ 4 mm or 6 mm $\times$ 3 mm elliptical disk was dip coated 1 mm deep into a series of different concentration solutions of IPA and water or alternatively a solution of 50% soap and water as shown in Fig. 1.

Through dip coating, approximately 1 mg of the propulsion agent was applied to the back of each sphere and elliptical disk. The surface tension of 100% IPA is $\sigma = 22$ mN/m and the surfactant in the soap reduces the surface tension of water from $\sigma = 72$ mN/m to 30 mN/m [31]. For the case of 100% IPA in water, an initial Marangoni number of $\mathrm{Ma} = \frac{\Delta\sigma D_{\mathrm{sphere}}}{\mu D_{\mathrm{Diffusion}}} = 3 \times 10^8$ suggests that the motion of the spheres will be dictated by the induced Marangoni flow and that diffusion of the IPA will have little effect. Here, $\Delta\sigma$ is the surface tension difference over dominant length scale in this problem, D_{sphere}, μ is the viscosity of water and $D_{\mathrm{diffusion}} = 1 \times 10^{-9}$ m^2/s is the diffusion coefficient of IPA in water.

The spheres were made from polypropylene (PP) which has a density of $\rho = 920$ kg/m^3 and a contact angle with water measured to be 70 deg. A 2.4 mm hole was drilled into the top of each sphere to a depth of 3 mm in order to reduce the mass of the sphere by 10% so it would float more easily. The hole was also used to change the center of mass of the sphere so that it would float with a preferred orientation with the hole opening facing up. As it floated, 4.5 mm of the sphere was below the air–water interface and the interface around the sphere was found to have a strong convex interfacial curvature with a radius of curvature measured optically from a side view of the sphere to be $R = 0.5$ mm. This radius of curvature was found to be the same on both the upstream and downstream side of the spheres and was not affected by the addition of IPA or soap. Elliptical disks of two different aspect ratios were also fabricated for shape comparative study. For an elliptical disk of aspect ratio, AR = 1.5, the minor axis was $D_{\mathrm{minor}} = 4$ mm and major axis was $D_{\mathrm{major}} = 6$ mm whereas for an elliptical disk of AR = 2, the minor axis was $D_{\mathrm{minor}} = 3$ mm and major axis was $D_{\mathrm{major}} = 6$ mm. The elliptical disks were $t = 1.5$ mm thick. The elliptical disks were fabricated from polydimethylsiloxane (PDMS). PDMS has a density of $\rho = 965$ kg/m^3 and, as a result, within the optical resolution of the camera, the interface around the floating elliptical disk was found to remain flat.

To begin an experiment, the spheres and the elliptical disks were carefully placed on to the air–water interface with tweezers. From the initial contact of the spheres and elliptical disks on the surface of the water to release from the tweezers took approximately 0.2 s. To average out any errors resulting from fabrication, dip coating or surfer placement, all measurements were repeated at least five times using a minimum of three different spheres or elliptical disks to minimize bias errors due to fabrication. In order to track the motion of the Marangoni surfers, a video camera was used capture the particle motion at a frame rate of 17 fps. These videos were then analyzed using a particle tracking software (Tracker) to obtain the velocity profile of the spherical and elliptical disk-shaped Marangoni surfers as a function of time. PIV measurements were obtained by first seeding the water with 40 μm diameter hollow silvered glass spheres, illuminating the PIV particles with a 0.5 mm thick light sheet from a Argon-ion laser, capturing the motion of the PIV particles using a high-speed video camera (Phantom v4.1) at 100 fps and correlating their motion using a commercially available PIV software (LaVision)
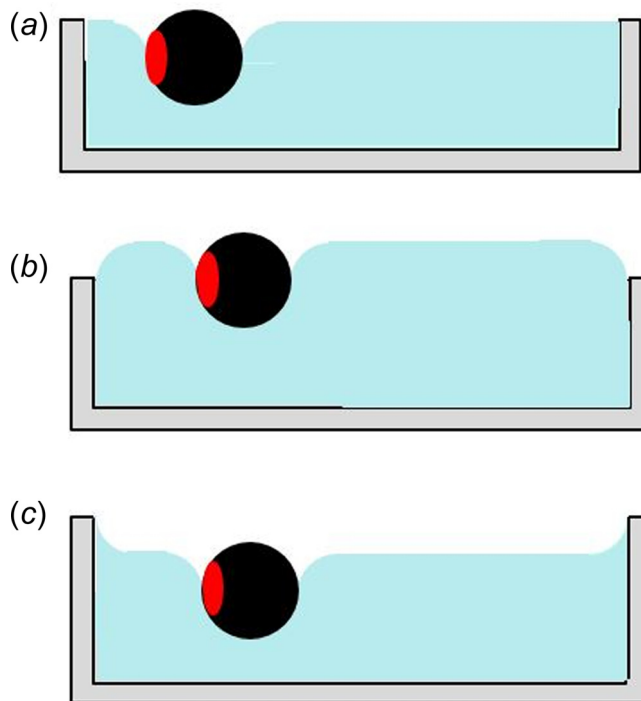

Fig. 2 Schematic diagram of the interactions between a dense particle floating on an air–water interface with (a) flat, (b) convex, and (c) concave curvature along the outer wall of the dish

[6]. Two different image planes were illuminated with the laser light sheet. The first was the xy-plane at the air–water interface to measure the interfacial flow. The second was the xz-plane passing through the center of the surfers from below to measure the flow directly underneath the surfer.

The effect of interface curvature was investigated by using a significantly smaller Petri dish $D = 86$ mm. Three different curvatures at the edge of the Petri dish were investigated—flat, convex, and concave as shown in Fig. 2. To obtain the desired interface curvature, the Petri dish was first fully filled so that the contact line could be pinned to the top edge of the Petri dish and the interface forced to be perfectly flat in Fig. 2(a). With the help of a syringe, 9 ml of water was either added or withdrawn to produce either a convex or concave interface, respectively. Using this technique, optical measurements showed that a radius of curvature of approximately $\mathcal{R} = 1.0$ mm was repeatedly obtained at the edges of the Petri dish for each concave or convex experiment performed.

3 Results and Discussion

3.1 Motion of Spherical Marangoni Surfers Propelled by Soap. In this section, the motion of a spherical Marangoni surfer using a soap solution as the propulsion agent was investigated. As described in Sec. 2, 1 mm of the sphere was dip coated in a solution of 50% soap and water. After the sphere was deposited onto the air–water interface, the surfactants diffused from the sphere into the bulk and very quickly began to populate the air–water interface thereby reducing its interfacial tension to $\sigma = 30$ mN/m in regions where the air–water interface was saturated with surfactant. It is expected that the minimum surface tension along the interface should arise close to the back of the sphere where it was coated with soap. The Marangoni flow produced as a result of the surface tension gradient drives the motion of the sphere. A straight-line translational motion of the sphere was observed without rotation for the case of soap. As seen in Fig. 3, upon its release, the sphere, initially accelerated to a velocity of $U_{\mathrm{sphere}} = 18$ mm/s after a time of $t = 0.5$ s before beginning to
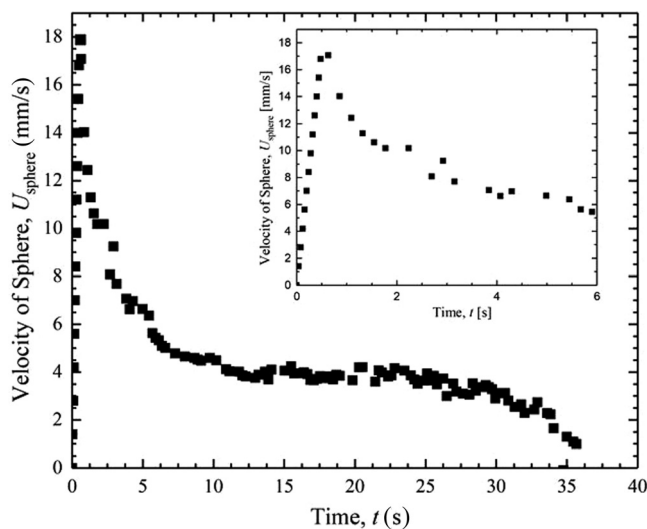
Fig. 3 Plot of the sphere velocity, U_{sphere}, as a function of time, t, for a spherical Marangoni surfer propelled by soap. Inset shows the nearly constant acceleration at early times.

decelerate. This corresponds to a maximum Reynolds number of, $\text{Re} = \rho U_{\text{sphere}} D/\mu = 114$. During the initial 0.5 s, a constant acceleration of $a = 37\,\text{mm/s}^2$ was found. Between $0.5\,\text{s} < t < 5\,\text{s}$, the sphere decelerated as the release rate of surfactant decayed with time and the strength of the Marangoni flow diminished. After roughly $t = 5\,\text{s}$, the sphere was observed to reach a steady-state velocity of $U_{\text{sphere}} = 4\,\text{mm/s}$ ($\text{Re} = 25$) which it maintained for more than 25 s before colliding with the wall of the Petri dish. At long times, it appears that a constant release rate of the soap from the sphere to the interface was obtained. The duration of this steady-state translational motion was found to be a function of the concentration of soap applied to the sphere, the release rate of soap into the water and, of course, the distance the sphere has available to travel due to size constraints of the Petri dish. Similar observations of steady-state straight-line motion were observed for similarly sized circular disks propelled by soap in our previous experiments [6]. In those experiments, maximum and steady-state velocity of the circular disks were all within 10% of what was observed here for the spheres. However, the acceleration of the spheres was found to be more than 50% larger than the circular disks.

It is also important to note that, in these experiments, convection and not diffusion dictates the details of the surfactant concentration field. There is little to no diffusion of surfactant molecules across streamlines. This conclusion is drawn from the large Peclet number of these experiments, $\text{Pe} = D_{\text{sphere}} U_{\text{sphere}}/D_{\text{diffusion}} \sim 10^5$. Here, $D_{\text{diffusion}} \sim 10^{-9}\,\text{m}^2/\text{s}$ is the approximate diffusion coefficient for the two surfactants in the soap, sodium laureth sulfate, and sodium lauryl sulfate.

3.2 Particle Image Velocimetry of a Spherical Marangoni Surfer Propelled by Soap. The PIV vector field measurements of the flow in the water around a spherical Marangoni surfer propelled by soap are presented here. In Fig. 4, PIV measurements of the interfacial flows around the sphere is shown for the sphere as it moves with a steady-state constant velocity. This snapshot in time was taken from the time window between $t = 15\,\text{s}$ and 20 s in Fig. 3. The motion of the sphere in Fig. 4(a) is from left to right. In Fig. 4(a), a stagnation point was observed approximately one diameter from the soap-coated trailing edge of the sphere. From that stagnation point, a dilational interfacial flow field was observed. Although we have no explicit evidence, it is likely that the stagnation point in the PIV data corresponds to the location of the maximum soap concentration and the thus the minimum in the
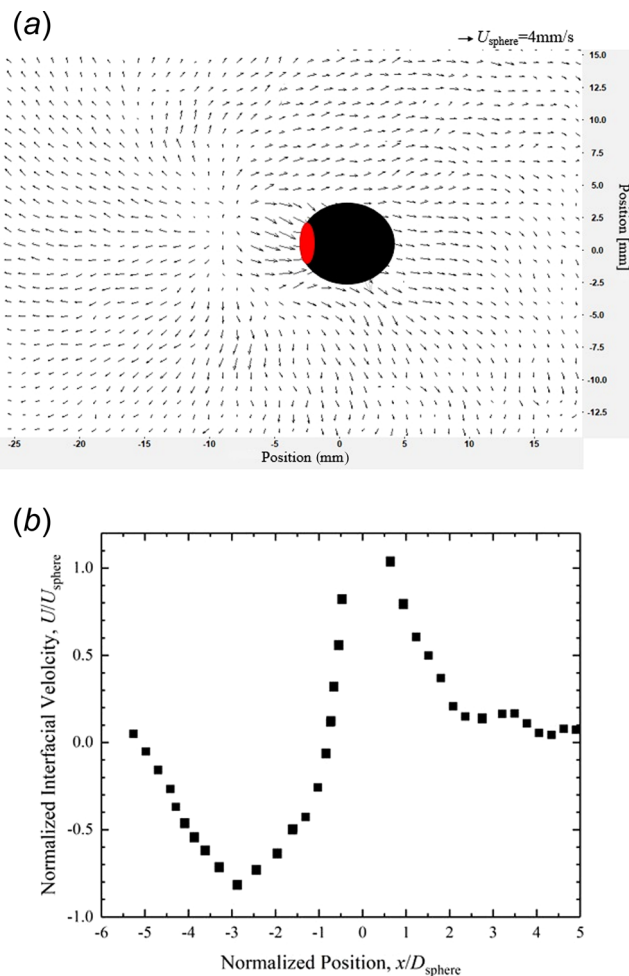

Fig. 4 (*a*) PIV measurements of the steady-state velocity vector field around a floating sphere propelled by Marangoni stresses induced by the release of soap released from the sphere. The area of the sphere coated with soap is shown in red. (*b*) Normalized centerline flow velocity, U/U_{sphere}, as a function of normalized position, x/D_{sphere}. The velocity of the sphere is $U_{\text{sphere}} = 4\,\text{mm/s}$ and its center is located at (0,0).

surface tension. The location of the stagnation point is counterintuitive. Due to the high concentration of soap on the trailing edge of the sphere, we would expect the surface to dilate from a location very close the trailing edge of the sphere if not directly adjacent to it. As discussed in Sur et al. [6], it is important to note that there is a finite time required for the surfactant to diffuse to and then adsorb onto the air–water interface.

During the adsorption time, t_{ads}, the sphere will move a finite distance, $L = U_{\text{sphere}} t_{\text{ads}}$. This argument suggests that the minimum interfacial tension will not exist adjacent to the trailing edge of the sphere, but instead it will appear a millimeter or more downstream of the sphere.

The velocity profile along the centerline of the sphere is shown in Fig. 4(*b*). For clarity, the interfacial velocity is normalized by the sphere velocity, U/U_{sphere}, and the position along the centerline is normalized by the sphere diameter, x/D_{sphere}. In both Figs. 4(*a*) and 4(*b*), the center of the sphere has been placed at $(x,y) = (0,0)$. The centerline velocity profile in Fig. 4(*b*), more clearly shows the presence of the stagnation point at a position of $x/D_{\text{sphere}} = -0.9$. For comparison, in Sur et al. [6] a stagnation point was also observed behind a circular disk propelled by soap. However, in their study, the nondimensional location of the stagnation point was found to be different at $x/D_{\text{disk}} = -1.5$. Although this is further in nondimensional form, the stagnation point
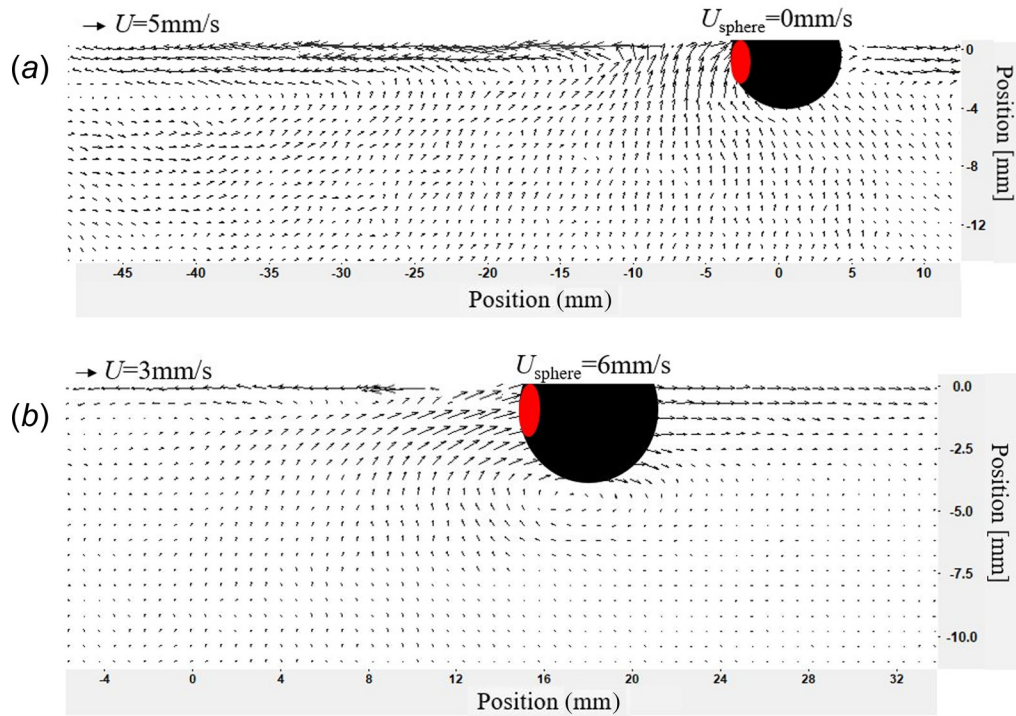
Fig. 5 PIV measurements of the velocity vector field underneath a floating sphere propelled by the Marangoni flow induced by soap released on the left side of the sphere in the area denoted in red for (*a*) a stationary sphere 0.5 s after immersing it in water and (*b*) for the sphere moving with a velocity of $U_{\text{sphere}} = 6$ mm/s at 0.5 s after it was released. A scale arrow is shown in each subfigure as reference.

observed in each case exists at a roughly the same physical distance of $x = 6$ mm downstream of the center of the circular disk and the sphere. Given that the velocity of the sphere and circular disk are similar in these experiments, this observation is consistent with the hypothesis that a finite time is needed for the surfactant to find and adsorb to the air–water interface.

Far from the sphere in its wake, the maximum velocity of the dilating interface was found to be slightly lower than the velocity of the sphere $U/U_{\text{sphere}} = -0.9$. Just upstream of the sphere, the maximum velocity was measured to be $U/U_{\text{sphere}} = 1.05$. This 5% increase over the sphere velocity produces a small relative flow velocity, which in addition to the traction force produced by the interfacial tension gradients, provides the necessary fluidic forces to overcome the friction and form drag on the submerged portion of the sphere. In the case of the circular disk, the relative velocity upstream and downstream of the circular disk was found to be approximately 5–10% higher as compared to spheres. This observation suggests that the floating sphere has a lower drag coefficient than the floating circular disk and highlight the impact that shape can have on the dynamics of relatively simply Marangoni surfers.

The three dimensionality of the flow field around the sphere was inter-rogated by changing the orientation of the laser light sheet, aligning it vertically, and passing it into the Petri dish from below. The PIV vector fields in Fig. 5 show the velocity profiles beneath the sphere along a plane that bisects the sphere along the direction of its motion. Note that, due to the curvature of the air–water interface around the sphere, visualizing PIV particles from the side of the Petri dish was difficult near the air–water interface. As a result, measurements of the velocity profile along the air–water interface in this orientation were difficult to measure and, as such, the data in Fig. 4 should be consulted for the most accurate measurements of the interface velocity. The focus of the data in Fig. 5 is to highlight the flow velocity beneath the sphere and several millimeters below the interface. In Fig. 5, PIV

measurements are presented for a stationary sphere and a sphere shortly after its release. In Fig. 5(*a*), the PIV measurements for the flow underneath the stationary sphere is presented 0.5 s after the sphere was inserted onto the water interface. A wide, shallow start-up vortex rotating clockwise can be observed in the wake of the sphere. The center of the vortex was found to move away from the sphere with time at a speed of 2 mm/s. As time progressed, the strength of the vortex strength was found to decrease. The magnitude of the vorticity of the vortex was found to be $\omega = 10\,\text{s}^{-1}$ at $t = 0.2\,\text{s}$ and to $\omega = 4\,\text{s}^{-1}$ at $t = 1\,\text{s}$. The vortex observed beneath the sphere is weaker than the vortex previously observed beneath a stationary circular disk [6].

A strong upward flow was observed below the sphere with the vertical velocity appearing on the side of the sphere where the surfactant was applied and where the stagnation point was observed along the interface. This vertical flow is required to satisfy continuity around the stagnation point. The velocity of the upward flow was found to increase as the flow approached the interface, eventually reaching a maximum velocity of $U = 8$ mm/s. The upward velocity is similar in magnitude to the maximum lateral interfacial velocity in the wake of the sphere which was found to be $U = 10$ mm/s. The velocity of the upward flow was approximately 30% less than that measured for a circular disk [6]. The lower upwelling velocity might be due to the more streamlined path available for flow to move into the wake of the sphere from below the sphere and from around the sides of the sphere. As a result, fluid is more easily supplied to replace the outgoing fluid along the dilating interface. For the case of the circular disk, the dilating interface was fed primarily by fluid coming from locations directly below the stagnation point.

In Fig. 5(*b*), the flow beneath the sphere is presented $t = 0.5\,\text{s}$ after the sphere was released on the air–water interface. The release process is not instantaneous, but takes roughly 0.15 s from deposition to release from the tweezers. As a result, a Marangoni flow similar to the PIV vector field in Fig. 5(*a*) will have already
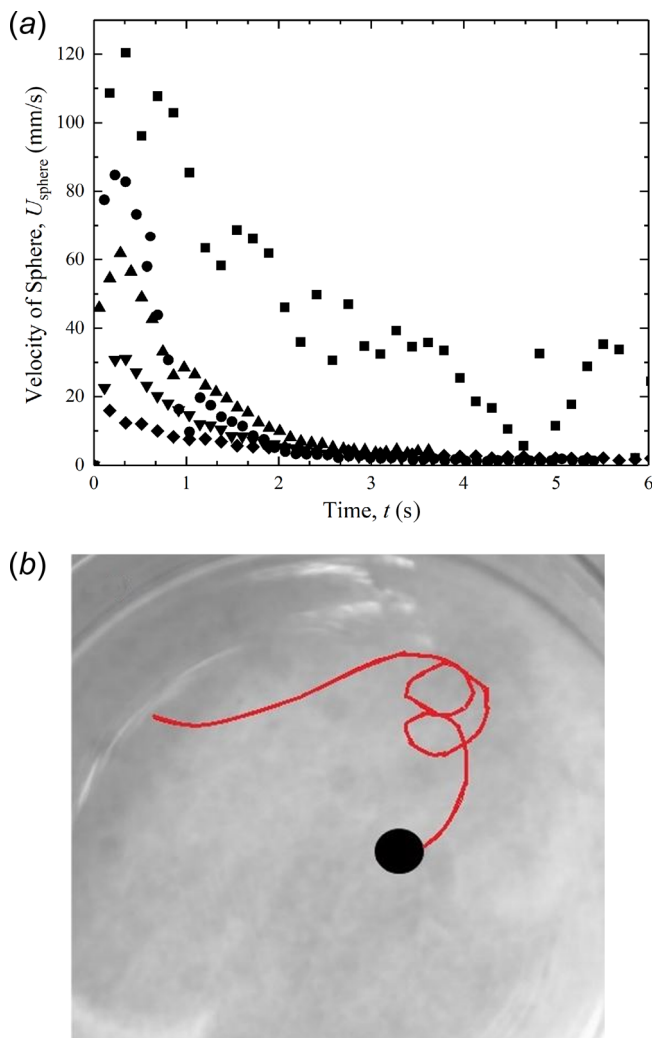
(a)

(b)

Fig. 6 (*a*) Plot of velocity of a sphere, U_{sphere}, with time, t, for IPA strength of (♦) 20 wt %, (▼) 30 wt %, (▲) 40 wt %, (●) 50 wt %, and (■) 100 wt % and (*b*) the figure on the right showing the trajectory of the sphere for the case of 100 wt % IPA

begun to setup before the sphere is fully released from the tweezers. This is one reason why we felt it was important to show the no-flow case in Fig. 5(*a*). The PIV vector field in Fig. 5(*b*) shows the presence of a stagnation point in the wake of the sphere and also a region of weak recirculation, $\omega = 4\,s^{-1}$, right beneath the sphere as the sphere achieved a velocity of $U_{sphere} = 6\,mm/s$. Under similar flow conditions, a recirculation area was also observed beneath the circular disk Marangoni surfers. However, in that case, the attached vortex was much more well defined with a significantly larger vorticity, $\omega = 16\,s^{-1}$ [6]. In addition to the attached vortex beneath the sphere, a counter-rotating start-up

vortex downstream of the sphere was also formed upon release. As time progressed, the start-up vortex was shed and convected downstream of the sphere by the dilating interface as was observed for the case of the stationary sphere.

3.3 Motion of Spherical Marangoni Surfers Propelled by Isopropyl Alcohol. In order to investigate the effect of propulsion strength, the propulsion agent was changed from soap to IPA. Although the surface tension of IPA and an air–water interface saturated by soap are similar, because IPA is a smaller and more-mobile molecule than the surfactants used in soap, it can quickly change the local surface tension behind the sphere resulting in a fast-acting and intense propulsion. Unfortunately, the fast dynamics of IPA come with a negative cost as the IPA coated on the sphere was depleted quickly resulting in significantly shorter propulsion times and in some cases no observed steady-state velocity. The velocity profiles for a series of spheres propelled by Marangoni stresses induced by the presence of IPA in the wake of the sphere are presented in Fig. 6. The speed of the sphere and the Reynolds number of the flow was modified by systematically varying the concentration of the IPA in water solution from 100 wt % down to 20 wt %. Decreasing the IPA concentration was found to decrease both the strength and the duration of propulsion. For the case of 20 wt % IPA in water, a straight-line translational motion was observed. The maximum velocity of $U_{sphere} = 18\,mm/s$ and Reynolds number of Re = 110 were very similar to those observed for propulsion using soap. However, unlike the case of soap, the sphere was observed to come to rest after just $t = 4\,s$. No steady-state, constant velocity motion was observed for the 20 wt % IPA case nor was it observed for any of the cases using a higher IPA concentrations. This is a very different response from when soap was used as the propulsion agent, but consistent with the findings for disks although for the case of IPA, the maximum velocity attained by the sphere is more than 25% smaller than the velocity obtained by the disks [6].

Increasing the IPA concentration to 100 wt % increased the maximum velocity and Reynolds number of the sphere to $U_{sphere} = 120\,mm/s$ and Re = 760, respectively. The values of maximum velocity and Reynolds number are tabulated for each IPA concentration studied and can be found in Table 1. As was observed previously for the case of circular disks [6], a transition from an initial straight-line translational motion to a rotational orbital motion of the sphere was observed. Examples of the trajectories followed by surfers during a rotational orbital motion is shown in Fig. 6(*b*) for the case of 100 wt % IPA. As we will discuss in more detail in Sec. 3.5, through PIV measurements, the onset of rotation is the result of the shedding of one of a pair of separated vortices attached to the back of the sphere. The shedding of the vortex leads to an unbalanced lift force and a torque on the sphere that causes it to rotate. For Marangoni propelled spheres, this transition was observed when the concentration of IPA was increased from 25 wt % to 30 wt % and the resulting maximum sphere velocity and Reynolds number increased to $U_{sphere} = 40\,mm/s$ and Re = 255, respectively. With increasing maximum sphere velocity, the number of the rotations and the

Table 1 Velocities and Reynolds numbers obtained for spheres propelled by different concentration of IPA in water and soap

IPA concentration (wt%)	Maximum velocity, U_{max} (mm/s)	Maximum Reynolds number, Re_{max}	Velocity prior to rotation, U_{rot} (mm/s)	Reynolds number prior to rotation, Re_{rot}
100%	120 ± 5	760 ± 30	95 ± 5	600 ± 30
50%	85 ± 5	540 ± 30	60 ± 5	380 ± 30
40%	70 ± 5	430 ± 30	42 ± 3	265 ± 15
30%	40 ± 5	255 ± 30	15 ± 5	90 ± 30
25%	30 ± 5	190 ± 30	NA	NA
20%	18 ± 3	110 ± 15	NA	NA
Soap	15 ± 3	90 ± 15	NA	NA

angular velocity of the sphere during its rotations were found to increase. In all cases, rotation was found to occur after the peak velocity was achieved and during the deceleration of the sphere. The increased number and speed of the rotations with increasing IPA concentration is likely due to the larger velocity of the sphere at the onset of rotation.

For the 30 wt % cases, on average, the sphere reached a maximum velocity of $U_{sphere} = 40$ mm/s corresponding to a Reynolds number of Re = 255 before beginning to decelerate. After decelerating for roughly 0.5 s to a velocity of $U_{sphere} = 15$ mm/s and a Reynolds number of Re = 90, the sphere was observed to spin. Note that, even though the peak Reynolds number for the stable 25 wt % IPA case (Re = 190) was larger than the Reynolds number observed prior to rotation for the unstable 30 wt % case, the sphere was not found to rotate. Thus, it appears that, rotation of the sphere requires a maximum Reynolds number greater than or equal to $Re_{max} \geq 255$ to be achieved. However, because the motion is transient, we felt it important to list both the maximum Reynolds number that was achieved and the Reynolds number at which rotation was first observed as a function of IPA concentration in Table 1. For comparison, the 1 mm thick circular disk-shaped Marangoni surfers studied in Sur et al. [6] were found to transition from translational to rotational motion if a peak Reynolds number greater than or equal to $Re_{max} \geq 180$ was achieved. For that specific case, rotation was first observed after the disk decelerated to a Reynolds number of $Re_{rot} = 120$ [6]. Thus changing the shape of the Marangoni surfer from a circular disk to a sphere clearly affects the stability of the Marangoni surfer. Based on the 50% larger value of the maximum Reynolds number achieved without rotation, the sphere was found to be more stable as compared to the circular disk.

3.4 Motion of an Elliptical Disk Marangoni Surfers Propelled by Isopropyl Alcohol.

In order to better understand the role of the shape and symmetry of the Marangoni surfer, a series of thin disks with elliptical shapes were studied. Here, the dynamics and stability of an elliptical disk propelled by IPA was investigated for two different aspect ratios, AR = 1.5 and AR = 2.0, and two different orientations with Marangoni propulsion aligned with the major and minor axis of the elliptical disk. As described in the experimental section, the elliptical disk with an aspect ratio AR = 1.5 had a major axis of $D_{major} = 6$ mm and a minor axis of $D_{minor} = 4$ mm, while the elliptical disk with aspect ratio AR = 2 had a major axis of $D_{major} = 6$ mm and a minor axis of $D_{minor} = 3$ mm. As shown in Fig. 1, the elliptical disks were dip coated in a variable concentration solution of IPA in water to a depth of 1 mm. Dip coating was performed in two orientation as shown in Fig. 1 to induce flow along the major axis, Fig. 7(a), or minor axis, Fig. 7(b). For the two different aspect ratio elliptical disks, the velocity profile had the same general character. The elliptical disks were found to accelerate quickly, go through a maximum within the first 0.25 s and decay to zero after 2 or 3 s. For case of 100 wt % IPA shown in Fig. 7, a series of local maxima can be seen during its deceleration phase. These peaks indicate times during which the vortices in the wake of the elliptical disks were shed and a transition from straight-line to rotational motion was observed.

For the case of an elliptical disk with AR = 1.5, at any a given concentration of IPA, the maximum velocity achieved while translating along the minor axis of the elliptical disk was consistently 40% lower than the maximum velocities achieved while moving along the major axis of the elliptical disk. For the case of 100 wt % IPA, a maximum velocity of $U_{ellipse} = 170$ mm/s was achieved along the major axis whereas a maximum velocity of $U_{ellipse} = 120$ mm/s along the minor axis. This difference in velocity is due to the higher drag experienced by an elliptical disk during its motion along the minor axis as the object is more bluff and less streamlined. Although the physics are not the exactly the same as here, similar difference in the drag coefficient can be
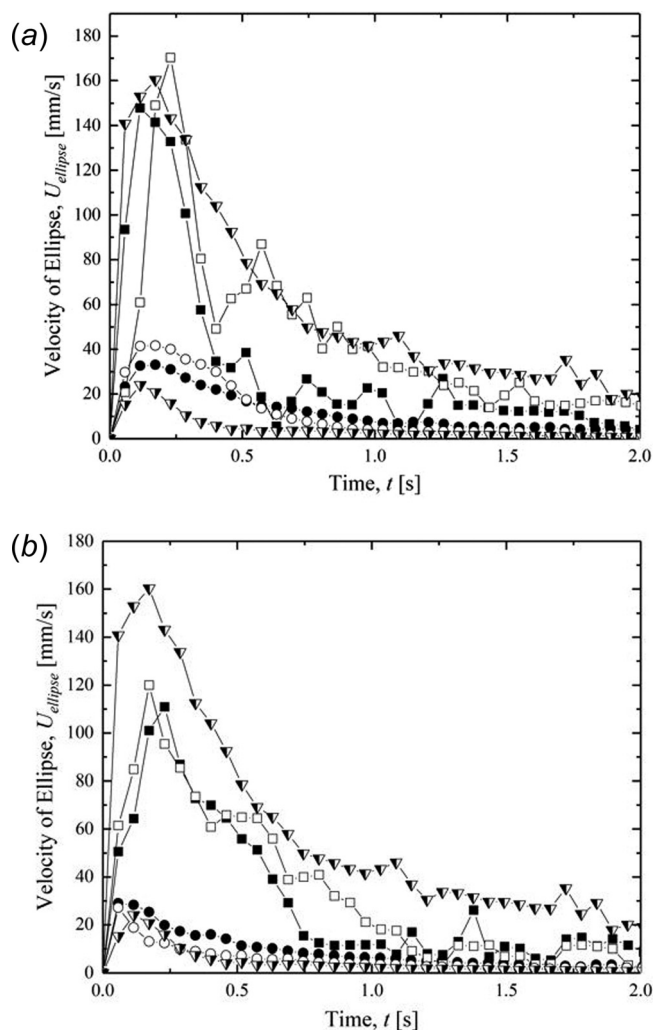

Fig. 7 Velocity of an elliptical disk, $U_{ellipse}$, as a function of time for (●) 20 wt % IPA in water and (■) 100 wt % IPA. Data include motion along (a) the major axis and (b) the minor axis of the ellipse. Filled symbols correspond to aspect ratio AR = 1.5 while hollow symbols correspond to AR = 2. For completeness, data for a cylindrical disk (AR = 1) are also plotted for (▽) 100 wt % IPA and (△) 20 wt % IPA in water. The data for the AR = 1 case were reproduced with permission from Ref. [6].

found based on the orientation of an elliptical cylinder in uniform cross flow [32].

Along with variation in the maximum velocity, the aspect ratio and orientation of the elliptical disk was found to have a substantial effect on the stability of the surfer. For all the different aspect ratio elliptical disks tested, translational motion along the minor axis of the elliptical disk was found to be more stable than motion along its major axis. The critical velocities and Reynolds number for rotation are presented in Table 2 for the AR = 1.5 and AR = 2 elliptical disk and the circular disk (AR = 1) published previously [6]. As an example, take the AR = 1.5 elliptical disk. For motion along the major axis, the elliptical disk became unstable at maximum Reynolds number of $Re_{max} > 110$, whereas for motion along the minor axis this transition was observed at $Re_{max} > 250$. Here, Reynolds number is defined as Re = $\rho U L/\mu$, where $L = D_{minor}$ for motion along the major axis and $L = D_{major}$ for motion along the minor axis. Increasing the aspect ratio of the elliptical disk from AR = 1.5 to AR = 2 was found to destabilize the motion along both the major and the minor axis. From Table 2, it can be observed that the transition from a linear translational motion to a rotational motion for the AR = 2 elliptical disk was observed at

Table 2 Velocities and Reynolds numbers achieved for a several different concentration of IPA used to propel elliptical disks with aspect ratios between $1 \leq AR \leq 2$ along the major and minor axis

IPA concentration (wt%)	Maximum velocity, U_{max} (mm/s)	Maximum Reynolds number, Re_{max}	Velocity prior to rotation, U_{rot} (mm/s)	Reynolds number prior to rotation, Re_{rot}
Motion along major axis, AR = 1.5				
100%	155 ± 5	620 ± 20	110 ± 15	400 ± 40
25%	45 ± 5	180 ± 20	25 ± 5	100 ± 20
20%	27 ± 3	107 ± 11	NA	NA
Motion along minor axis, AR = 1.5				
100%	110 ± 10	660 ± 60	80 ± 5	480 ± 30
30%	55 ± 5	330 ± 30	25 ± 5	150 ± 30
25%	40 ± 5	240 ± 30	NA	NA
Motion along major axis, AR = 2				
100%	170 ± 10	510 ± 30	140 ± 5	435 ± 15
20%	40 ± 5	120 ± 15	25 ± 5	75 ± 15
10%	20 ± 1	58 ± 3	NA	NA
Motion along minor axis, AR = 2				
100%	110 ± 10	660 ± 60	90 ± 5	540 ± 30
25%	40 ± 5	240 ± 30	20 ± 5	120 ± 30
20%	25 ± 3	160 ± 17	NA	NA
Motion of a cylindrical disk, AR = 1				
100%	160 ± 8	640 ± 30	120 ± 10	450 ± 35
25%	45 ± 5	180 ± 20	30 ± 5	120 ± 20
20%	28 ± 2	112 ± 8	NA	NA

The data for AR = 1 were reproduced with permission from Ref. [6].

just $Re_{max} > 60$ for motion along the major axis and $Re_{max} > 140$ for motion along the minor axis. The stability of the elliptical surfers appears to be extremely sensitive to changes in aspect ratio. With a 25% reduction in the aspect ratio from AR = 2 to AR = 1.5, a 100% increase in the critical Reynolds number was observed for flow along the two principle axes. Reducing the aspect ratio even further to a circular disk with AR = 1 was previously shown to transition to rotation at a critical Reynolds number of $Re_{max} = 180$ [6], while for the sphere presented in Sec. 3.3, the critical Reynolds number was Re = 255.

Accompanying the decrease in stability, an increase in the rotation rate of the elliptical disk was observed with increasing aspect ratio for motion along both orientations. Here, for example, we compare the rotation rate for 100 wt % IPA case. For the case of an elliptical disk with AR = 1.5, the rotation rate was found to be $\omega = 6 \pm 1$ rot/s and $\omega = 3 \pm 1$ rot/s when along the major and minor axis, respectively. As the aspect ratio of the elliptical disk was increased to AR = 2, the rotation rate was found to increase substantially to $\omega = 9 \pm 2$ rot/s and $\omega = 4 \pm 1$ rot/s along the major and minor axis, respectively. A closer look at the surfer's motion shows a difference between the path profile followed by an elliptical disk and a symmetric surfer like a disk or a sphere. For the case of an elliptical disk, the surfer was found to rotate about its center of mass spinning in place like a top. For the case of the symmetric disks or spheres, the center of mass of the surfers were observed to trace out long slow circular paths. This difference also show up in the rotation rate of the surfer as the symmetric disk and sphere were found to rotate much slower at $\omega = 0.8 \pm 0.2$ rot/s and $\omega = 0.2 \pm 0.1$ rot/s, respectively. Thus, from these observations, a high aspect ratio elliptical disk designed to translate along its major axis would be an excellent design for a high efficiency Marangoni propelled rotor or mixer [7,33,34].

3.5 Particle Image Velocimetry of a Spherical Marangoni Surfer Propelled by Isopropyl Alcohol. In order to better understand the origin of the rotational motion of the spherical Marangoni surfers, PIV measurements of the velocity vector field around the spheres propelled by IPA were performed. In Fig. 8, the velocity vector field along the interface surrounding a stationary sphere, $U_{sphere} = 0$ mm/s, is presented. The sphere held stationary using tweezers fixed to a rigid stage. As was observed in Sec. 3.2 for the case of soap, a radially outward flow was observed originiating near the location where the IPA was applied to the sphere. However, the resulting flow pattern is very different from the case of soap presented in Fig. 4(a). Here, a pair of counter-rotating vortex can be observed in Fig. 8(a) on either side of the sphere just upstream of its equator. These vortices were observed to grow more distinct as time progressed until the supply of IPA was depleted from the sphere, but they were never observed to shed. The appearance of these vorticies is counterintuititve. Due to the direction of the surface tension gradient, one expects the flow to be radially outward everywhere including in the region upstream of the sphere. However, it is the interfacial tension gradient that in fact drives this flow as large influx of fluid from beneath and around the sphere is needed to conserve mass as the interface quickly dilates from the wake of the sphere, where the surface tension is minimized. The influx of fluid into to wake of the sphere can be seen more clearly from beneath the stationary sphere in Fig. 8(b). The presence of the sphere clearly acts as an obstacle to interface dialation. Our experiments have shown that if the sphere were removed and a drop of IPA were applied to the surface with a dropper, a purely radially outward flow would result from the location of the IPA application. Recall that in the case of soap, these vortices were not observed. The main difference between the soap and IPA is the flow strength. For the case of IPA, interfacial velocities as large as 50 mm/s were measured whereas for soap interfacial velocities no more than 15 mm/s were obtained. We will see that this difference in the flow strength also changes the dynamics of the motion of the sphere once it is released. In Fig. 8(b), the Marangoni flow field beneath the stationary sphere is also presented. Note the presence of a strong start-up vortex that has been shed and is moving away from the sphere. A similar start-up vortex was also observed for the stationary sphere propelled by soap. In each case, the strength and vorticity of the vortex were found to decay with time and distance from the sphere.

In Fig. 9, the Marangoni flow around a sphere moving at $U_{sphere} = 20$ mm/s is presented. Here, the sphere is propelled by 100 wt % IPA. The reversed flow observed upstream of the stationary sphere in Fig. 8(a), is not observed for the moving sphere
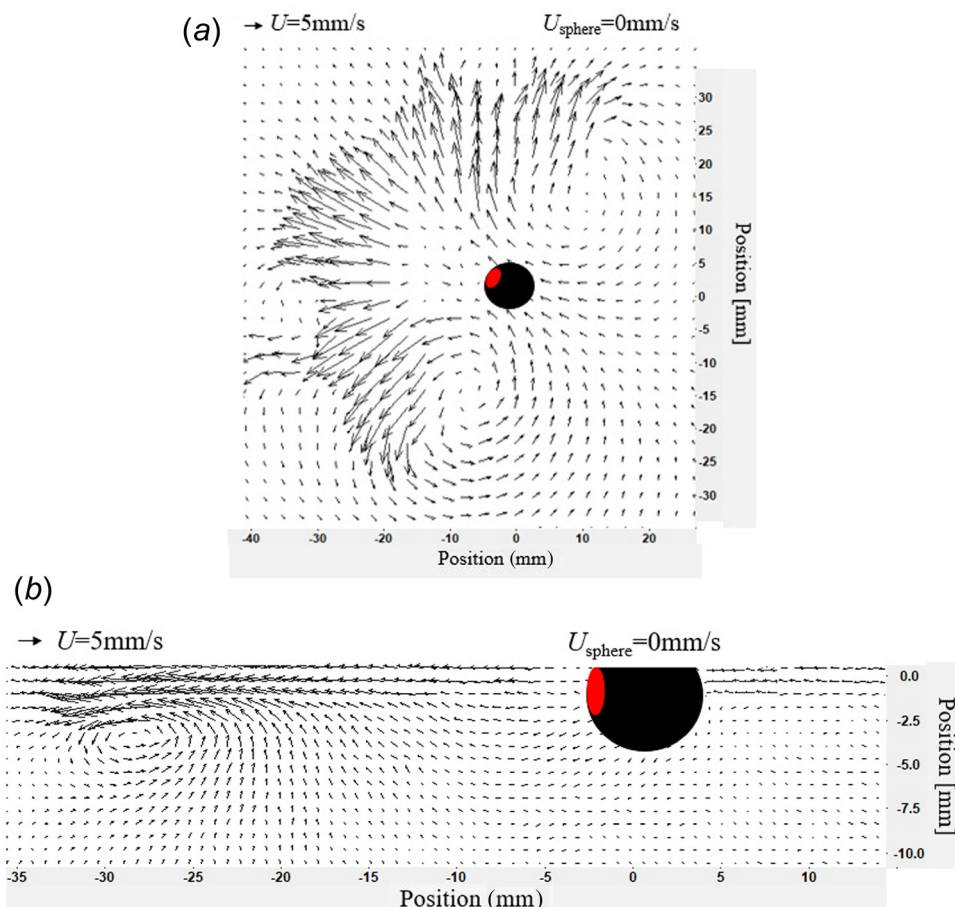
Fig. 8 PIV measurements of the velocity vector field (*a*) on the interface surrounding a stationary sphere (U_{sphere} = 0 mm/s) and (*b*) below a stationary sphere. The Marangoni flow is induced by the release of 100% IPA from the area of the sphere denoted in red. The figure corresponds to a time *t* = 0.5 s after the sphere was deposited on the surface of the water.

in Fig. 9(*a*). Instead, a strong flow is observed to emanate from the wake of the sphere where the surface tension is minimized by the high concentration of IPA. This flow can be observed to pass by the sphere and convect the sphere in the direction of high surface tension.

The interfacial vortices observed in Fig. 8(*a*) for the stationary sphere do form at early times, but quickly shed as the sphere is released from the tweezers and allowed to freely move along the interface. As seen in Fig. 9(*a*), two new counter-rotating vortices were observed to form near the equator of the sphere. These vortices are clearly distinct from the vortices observed in Fig. 8(*a*) as they are rotating in the opposite direction. For all the IPA concentrations for which a straight-line translational motion was observed, these vortices were observed to remain attached to the sphere for the extent of the experiment. However, for concentrations of 30 wt % IPA and above these vortices were observed to shed.

The shedding of the left-hand side vortex in Fig. 9 resulted in a deflection of the sphere to the right and a clockwise orbital rotation motion of the sphere that persisted until the IPA was depleted and the sphere eventually came to rest. As the vortex was shed, a jet of fluid was observed to move past the sphere on the left-hand side crossing between the sphere and the shed vortex. Similar vortex shedding was observed for disk-shaped Marangoni surfers as well [6]. The experiments were performed multiple times for each IPA concentration tested. The results of those tests showed no bias in the rotational direction of the spheres or the order in which the vortices shed from the sphere.

PIV measurements from beneath the sphere are shown in Fig. 9(*b*). As the sphere was immersed in the water and subsequently released by the tweezers onto the interface, a startup vortex similar to that seen in Fig. 8(*b*), was produce in the wake of the sphere and quickly shed. In Fig. 9(*b*), the startup vortex can still be observed 25 mm downstream of the sphere, rotating counterclockwise. Unlike the case of the stationary sphere, a second vortex attached to the sphere appears for the case of the moving sphere. This attached vortex was observed to grow with time and to rotate in the clockwise, in the opposite direction of the start-up vortex. The location of this vortex is quite different from the case of the circular disk studied previously [6] and the elliptical disks that will be discussed in Sec. 3.5. For both those disks, the attached vortex was found to be offset toward the rear edge of the disk where it appeared to be pinned to the sharp 90 deg corner that forms the border between the bottom and sidewall of the disk. The strength of the vortex underneath the sphere was found to be just $\omega = 4\,s^{-1}$, which was less than half of the vorticity measured for the vortex beneath the circular disk, $\omega = 10\,s^{-1}$, at a similar velocity of $U = 20$ mm/s velocity [6].

3.6 Particle Image Velocimetry of an Elliptical Marangoni Surfers Propelled by Isopropyl Alcohol. In Fig. 10, the interfacial flow profiles around the two different aspect ratio and two different orientation elliptical shaped Marangoni surfers are directly compared to each other and to the interfacial flow profiles observed for the axisymmetric spheres and circular disks. All the
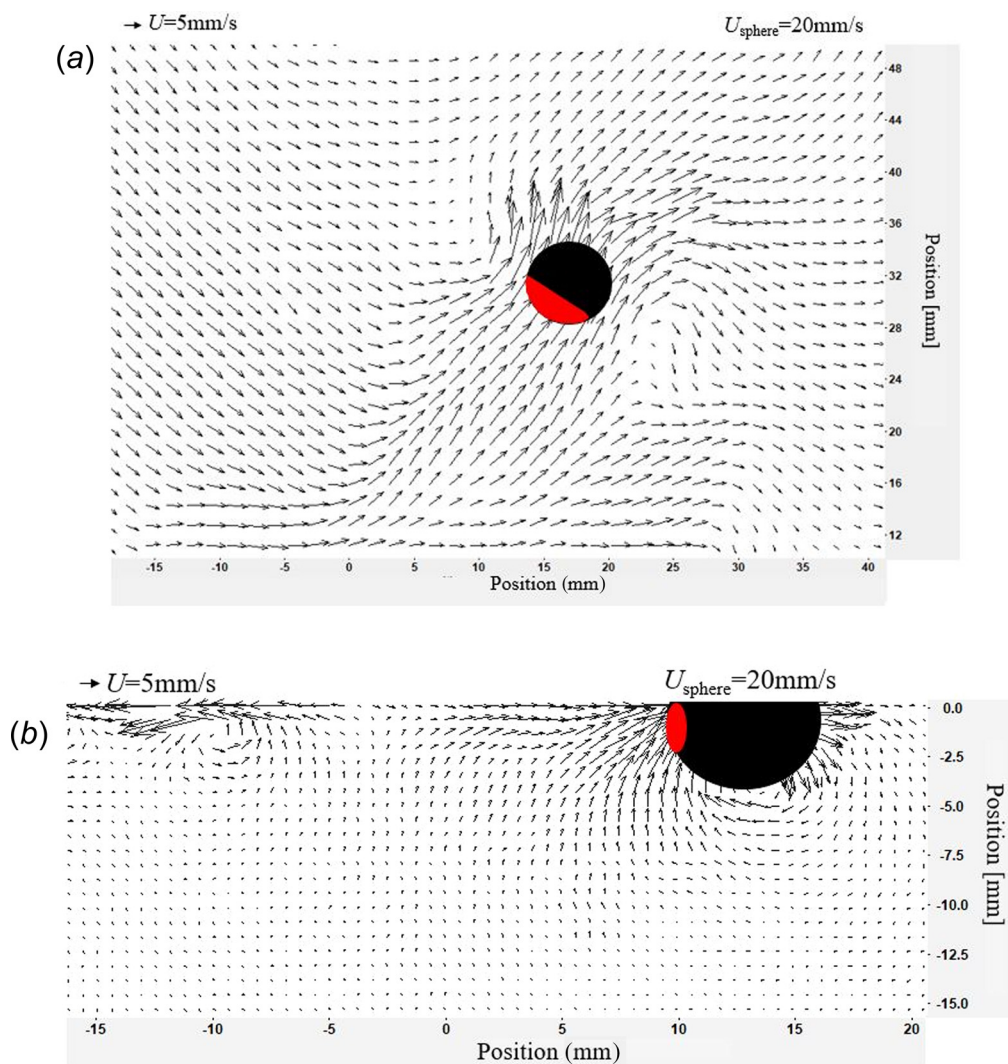
Fig. 9 PIV measurements of the velocity vector field (*a*) on the interface and (*b*) beneath a sphere moving at $U_{sphere} = 20$ mm/s at a time of $t = 1$ s after it was released. The instantaneous angular velocity was found to be $\omega = 6\,\text{s}^{-1}$. The Marangoni flow is induced by the release of 100% IPA from the area of the sphere denoted in red. The sphere was released at $(x, y) = (0, 0)$ in subfigure (*a*) and $(x,z) = (0,0)$ in subfigure (*b*).

PIV presented in Fig. 10 are for the case of 30 wt % IPA and were chosen to highlight differences in the flow field during the straight-line translational motion of each of the different Marangoni surfers. For all six cases, a pair of attached counter-rotating vortices can be observed to the sides of the surfers. It is evident from Fig. 10 that the position and strength of these vortices is affected by the shape and orientation of the surfer. For the case of the axisymmetric sphere described in Sec. 3.5 and the circular disk shown in the work of Sur et al. [6], the attached vortices were closely aligned with the equator of the surfer at $\theta = 83$ deg and $\theta = 85$ deg, respectively. The angle reported here is the angle measured between the velocity vector of the Marangoni surfer and the line bisecting the center of the Marangoni surfer and the attached vortices. As such, an angle of $\theta = 0$ deg corresponds to the direction of motion of the surfer. This is very different from the case of the nonaxisymmetric elliptically shaped surfers. While moving along either the major or the minor axis, the attached counter-rotating vortices are clearly located more toward the wake. For the case of the AR = 1.5 elliptical disk, while traversing along its major and minor axis, the vortices were found at $\theta = 135 \pm 4$ deg and $\theta = 125 \pm 3$ deg, respectively. Similarly, the location of the vortices for the AR = 2 elliptical disk were found

at $\theta = 123 \pm 2$ deg and $\theta = 115 \pm 3$ deg, respectively. The location of vortices may play a role on the change in the stability of the Marangoni surfers with shape. However, detailed numerical simulations are likely needed to fully understand the root causes of the change in stability with shape and orientation. One observation is clear, the increased torque arm resulting from the asymmetry of the elliptical surfers and the location of the vortices clearly amplifies the effect of vortex shedding by increasing the applied torque and dramatically increasing rotation rate of the surfer as the aspect ratio increases.

3.7 Effect of Interface Curvature on the Motion of Marangoni Surfers. In this section, the effect of interfacial curvature on the motion of both spherical and elliptical disk-shaped Marangoni surfers was investigated. For these experiments, IPA was used as the propulsion agent to generate the Marangoni flow. For both the spheres and the elliptical disks, an initial straight-line motion was observed. This can be seen in Fig. 11 for the spheres and Fig. 12 for the elliptical disks. Whether the Marangoni surfer continued along a straight-line trajectory into the wall or rotated away from the wall following an orbital path was found to depend on the
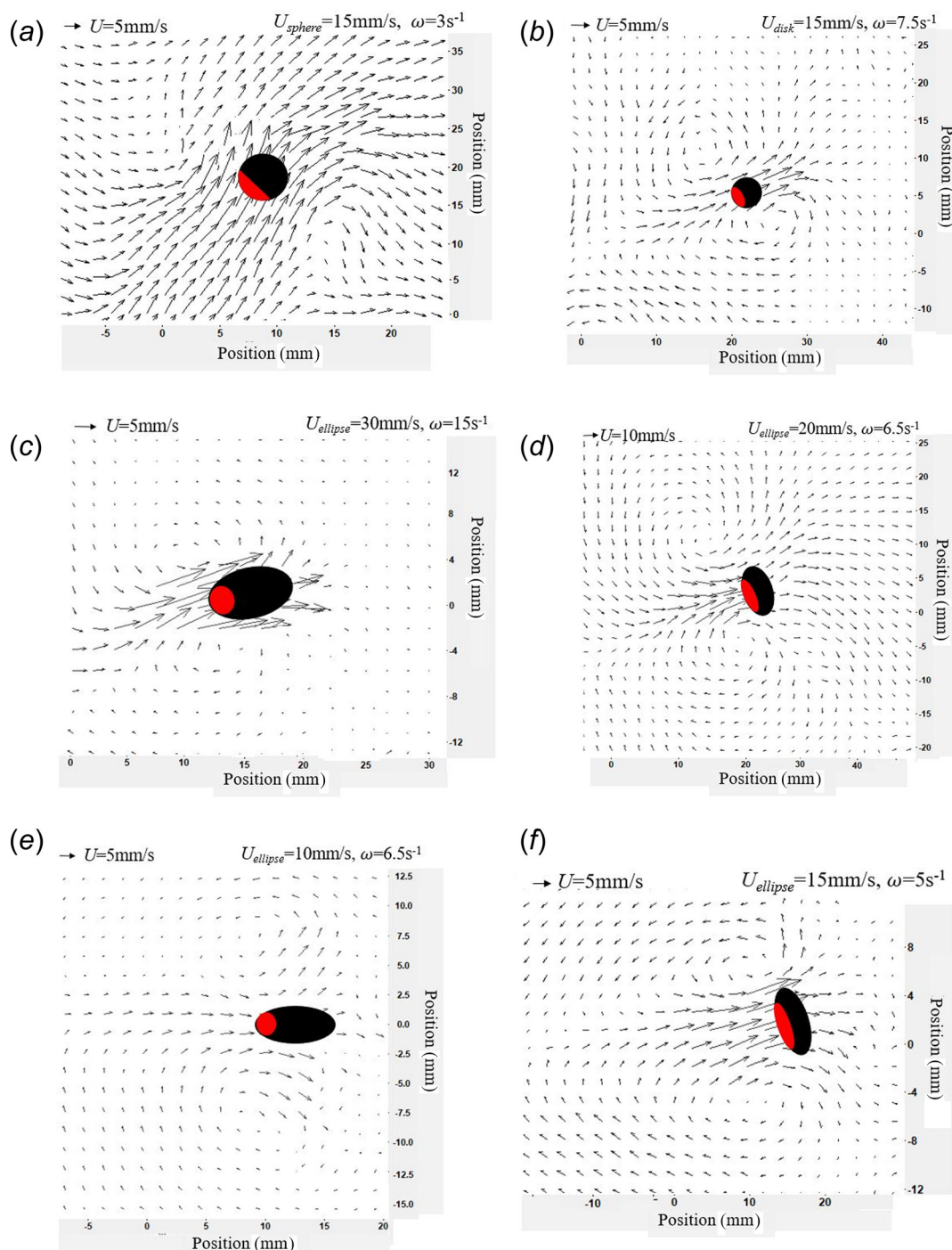
Fig. 10 PIV measurements of the velocity vector field upstream and downstream of a various Marangoni surfers. In all cases, 100 wt % IPA was released from the area on the surfer denoted in red. Data include vector fields around (*a*) a sphere, (*b*) a disk, (*c*) an elliptical disk (AR = 1.5) moving along its major axis, (*d*) an elliptical disk (AR = 1.5) moving along its minor axis, (*e*) an elliptical disk (AR = 2) moving along its major axis, and (*f*) an elliptical disk (AR = 2) moving along its minor axis.

shape and orientation of the surfer, the Reynolds number and the sign of the interface curvature at the wall.

An example of the trajectory of a spherical surfer approaching the boundary wall of the Petri dish along the flat interface is shown in Fig. 11(*b*). Provided the Reynolds number was large enough, the sphere was consistently observed to rotate and go through a series of orbital loops before eventually coming to rest. Compared to the unbound case, the peak Reynolds number needed to observe sphere rotation was reduced from $Re_{max} = 255$ to $Re_{max} = 190$ and the Reynolds number of the spherical surfer just

prior to the onset of rotation was reduced from $Re = 90$ to $Re = 60$. The presence of the wall clearly provides some additional destabilizing perturbation to the straight-line motion of the sphere even without interface curvature. This point is reinforced by the observation that a solution of 25 wt % IPA in water will cause rotation of the spherical surface on a flat, bounded interface, but will not on an unbounded interface. The physical origin of this difference is likely the presence of an adverse pressure gradient imposed upon the sphere as it approaches the boundary wall where both the interfacial and bulk fluid velocity must come to
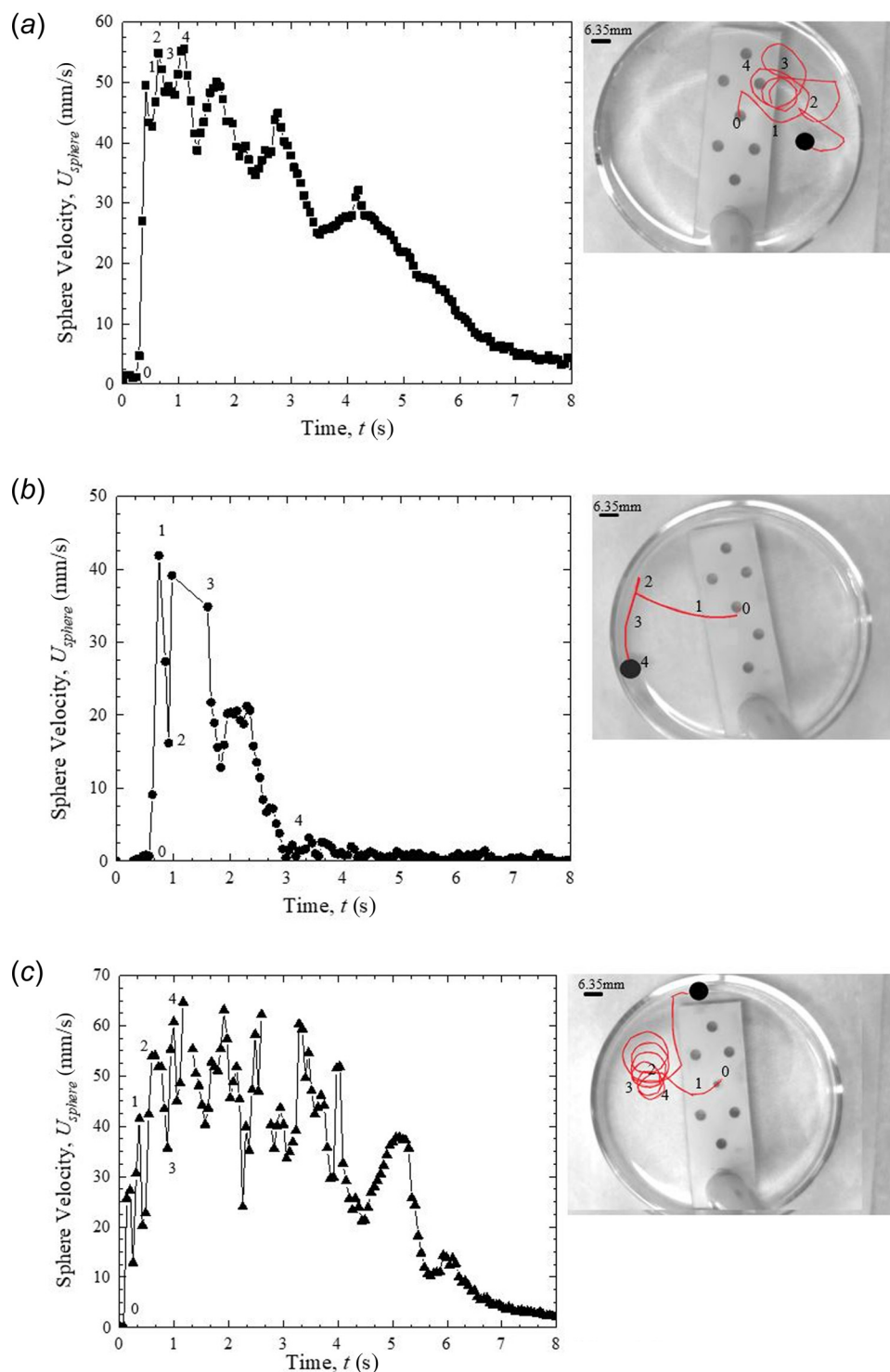
Fig. 11 Velocity profile of the sphere, U_{sphere}, plotted as a function of time, t, propelled along an air–water interface using 100 wt % IPA for (*a*) a flat, (*b*) a convex, and (*c*) a concave interface at the boundary of the Petri dish. A trace of the trajectory of the sphere is shown on the right.

rest. If the sphere does not approach the wall along a radial path, the pressure field will provide a torque that, at a high enough Reynolds numbers, can cause the sphere to rotate and the attached vortices observed in Fig. 10 to shed. Additionally, because of the interfacial curvature around the sphere, an additional repulsive force exists in this case because of the mismatch in curvature between the concave interface around the sphere and the flat interface present at the wall of the Petri dish. Both clockwise and counterclockwise orbit were observed depending on the

orientation of the particle as it approached the wall. A numbered sequence of labels has been used in Fig. 11(*a*) to highlight a series of peaks and valleys in the time history of the velocity data. Corresponding numbers have also been superimposed over the trajectories of the spherical surfer in Fig. 11(*b*) to illustrate how the velocities vary with time, space, and the phase within the rotational cycle. From the data, two velocity peaks can be observed per rotation of the sphere. This observation likely results from the fact that the orbital trajectories are not circular, but more elliptical
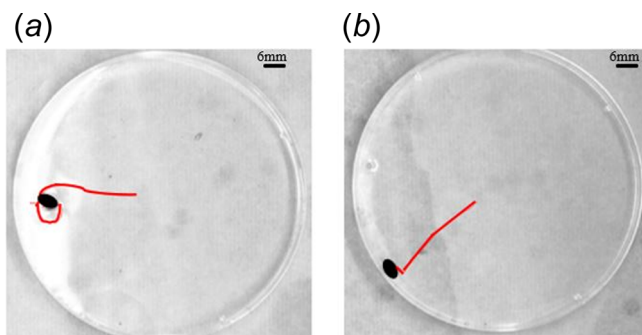
Fig. 12 The trace of the trajectory of interaction of an AR = 1.5 elliptical disk shaped surfer with a flat interface at the boundary for its motion along its (a) major axis and (b) minor axis

in nature. For case of 100 wt % IPA, the average radius of curvature of the orbital trajectories and the average period of rotation were found to be $R = 10 \pm 1$ mm and $T = 0.8 \pm 0.1$ s, respectively. It is important to note that the average angular velocity of the sphere as it approached the boundary, $\Omega = 10 \pm 2$ rad/s, was 50% larger than the angular velocity for the sphere rotating on an unbounded interface, $\Omega = 6 \pm 2$ rad/s.

The effect of a convex interface along the wall of the Petri dish on the trajectory of a spherical Marangoni surfer is shown in Fig. 11(b). As before, the sphere was observed to initially follow a straight-line motion toward the wall. However, as the sphere approached the wall along the convex interface, it did not rotate, but instead directly impacted the wall. The sphere was then observed to move along the wall in close proximity, never moving much more than a radius away from the wall before quickly came to rest. In this case, the curvature at the edge of the dish and around the sphere are both convex resulting in a capillary attraction that effectively bound the sphere in close proximity to the wall of the Petri dish. In addition to interfacial interactions, the convex curvature near the wall resulted in a decreased gravitational potential energy as the sphere moved to the wall resulting in an energy well that trapped the sphere and inhibited it from further motion away from the wall.

The effect of concave interfacial curvature along the wall of the Petri dish on the trajectory of a spherical Marangoni surfer is shown in Fig. 11(c). In this case, the sphere was found to begin a tight series of loops as it approached the wall. The mismatch in curvature between convex interface near the sphere and concave interface at the edge of the Petri dish provides an additional repulsive force and torque that destabilized the straight-line trajectory of the sphere. The average radius of curvature of the rotational motion and the average period of rotation for the concave case were found to be $R = 16 \pm 1$ mm and $T = 0.5 \pm 0.1$ s, respectively, resulting in an average angular velocity of $\Omega = 12 \pm 2$ rad/s. That is more than 30% larger than on the flat interface and twice as large as the angular velocity observed on an unconfined interface. This case, also highlights the main differences between the spheres, which have a convex interfacial curvature around them due to how they float and the circular disks studied previously [6] and the elliptical disks which will be discussed shortly, which do not deform the interface. Without the additional repulsion of the mismatch in interfacial curvature, the circular disk-shaped Marangoni surfers where found to follow a straight line motion directly into the wall along an interface with concave curvature without rotating or changing direction before impacting the wall [6].

In order to probe the effect of particle symmetry, shape, and orientation on the stability, the elliptical disks were also released in a small Petri dish of dimeter $D_{dish} = 86$ mm so that their interaction with a boundary could be studied and compared to the results for a spherical surfer. Unlike the experiments performed with the spherical surfers, the elliptical surfers are essentially neutrally buoyant in the water and do not distort the interface. As a result,

the strength of the interfacial curvature attraction and repulsion observed for the case of spheres are not expected to be as significant here. Thus, to simplify the discussion, the focus of the experiments for the elliptical surfers will be for the case of a flat interface along the wall of the Petri dish. In these experiments presented in Fig. 12, the elliptical surfers were propelled by 100 wt % IPA. For both the AR = 1.5 and AR = 2 elliptical disk, a similar result was observed. While moving along its major axes, the elliptical surfers were observed to deviate from their straight-line path and to start spinning as they approached the boundary wall. This can be seen for the AR = 1.5 elliptical disk in Fig. 12(a). Interestingly, under these very same conditions, the elliptical surfers traversing along their minor axes were not observed to spin. Instead, as seen in Fig. 12(b), these surfers approached the wall of the Petri dish maintaining a straight-line path before ultimately hitting the boundary wall and coming to rest. While attached to the wall, a Marangoni flow could still be observed as even though the particle had come to rest because the IPA coating the particle had not yet been depleted.

For the case of the AR = 1.5 elliptical disk traveling along its major axis, the peak Reynolds number was found to be $Re_{max} = 440 \pm 20$ and the Reynolds number prior to rotation was found to be $Re = 280 \pm 15$. Whereas, for the case of the AR = 1.5 elliptical disk traveling along its minor axis, the peak Reynolds number was found to be $Re_{max} = 450 \pm 10$ with no rotation observed. For the case of the AR = 2 elliptical disk traveling along its major axis, the peak Reynolds was found to be $Re_{max} = 330 \pm 15$ and the Reynolds number prior to rotation was found to be $Re = 240 \pm 10$. Whereas, for the case of the AR = 2 elliptical disk traveling along its minor axis, the peak Reynolds number was $Re_{max} = 480 \pm 20$ with no observed rotation.

The presence of a boundary does not appear to affect the stability of an elliptical surfer as long as it was traveling along its major axis. Rotation was observed for the same peak Reynolds numbers in both a bounded and unbounded domain. For example, if one compares the AR = 1.5 elliptical surfer with a peak Reynolds number of $Re_{max} = 440$ in a bounded and an unbounded domain, both surfers were observed to rotate after decelerating to the same Reynolds number, $Re = 280$. The presence of a flat interface near a boundary, similarly had no effect on the stability of circular disk studied previously [6]. This is very different from the results for the spherical surfer for which the presence of a mismatch in interfacial curvature near the bounding wall caused the surfer to be less stable and more likely to rotate even when moving along a flat interface.

Perhaps more interesting is the case of an elliptical surfer traveling along its minor axis. In this case, the presence of the bounding wall was found to significantly stabilize the straight-line translational motion for both aspect ratios studied. For example, an elliptical Marangoni surfer traveling along its minor axis on an unbounded interface was found to rotate once it reached a peak Reynolds number of $Re_{max} = 330 \pm 30$ and $Re_{max} = 240 \pm 30$ for an aspect ratio of AR = 1.5 and AR = 2, , respectively. For the bounded case, even at 100 wt % IPA and Reynolds numbers well above $Re > 400$, elliptical disk surfers traveling along their minor axis were never observed to rotate as they approached the boundary wall. This difference in stability is solely a result of the orientation of the elliptical Marangoni surfer

Although the physical origin for the enhanced stability of elliptical surfers traveling along their minor axis is not entirely clear, these results might have some utility. The improved stability of an elliptical disk while traversing along the minor axis can be used to direct Marangoni flow driven assembly [35,36]. This kind of assembly is quite different from the investigations performed on the assembly due to interface curvature, for which, the assembly between two particles is observed at the site of maximum deviatoric curvature [26,37]. As a result, for assembly driven by interfacial curvature, particles would assemble into a string of particles aligned along the major axis of the elliptical disks. For a neutrally buoyant elliptical surfer traveling along its minor axis, the

assembly will most likely occur side-to-side aligned along the minor axis of the elliptical disk. This side-to-side rather than tip-to-tip assembly provides new physical tool to guide self-assembly of objects along an interface and provides control over the spatial arrangements and final assembly of elliptical disk-shaped Marangoni surfers.

4 Conclusion

In the experiments presented in this paper, the dynamics of both spherical and elliptical disk-shaped Marangoni surfers were studied at moderate Reynolds numbers to better understand the role that particle shape, symmetry and orientation play on motion and stability. The Marangoni surfers were propelled by applying either soap or isopropyl alcohol through a dip coating process to the backside of each sphere and elliptical disk. Both IPA and soap were used to reduce the surface tension of water. The elliptical disks were neutrally buoyant and did not distort the air–water interface. However, due to the density, shape and contact angle with the water, the air–water interface around the spheres was deformed resulting in a convex interfacial curvature that helped support the unsubmerged weight of the spheres. The flow dynamics around the surfers was investigated through particle image velocimetry. In addition to studying the motion of the sphere and elliptical disks on an unconfined interface, the effect of the interaction between the surfers and the boundary with varying interfacial curvature was also investigated.

For the case of soap as the propulsion agent, the velocity of the surfers went through a maximum before a steady-state straight-line translation velocity was achieved. For the case of the sphere, a steady-state velocity and Reynolds number of $U_{sphere} = 4\,mm/s$ and a $Re = 25$ was achieved. However, for the case of IPA as the propulsion agent, a steady-state translational velocity was never achieved. In all cases, a fast acceleration, more rapid than the case of soap, was observed until a maximum velocity was achieved. Beyond this peak velocity, a continuous deceleration occurs until the motion had ceased. For the case of a sphere propelled by $100\,wt\%$ IPA, a peak velocity of $U_{sphere} = 120\,mm/s$ and a peak Reynolds number of $Re = 750$ was observed. For the case of an elliptical disk propelled by $100\,wt\%$ IPA, similar velocities were achieved when the elliptical disk was propelled along its minor axis. However, when the elliptical disk was propelled along its major axis, a 50% increase in velocity was observed due to its decreased drag coefficient. This variation in the maximum velocity clearly shows the effect of geometry and orientation can have on the steady motion of the surfers.

As the velocity of the surfers was increased with increasing concentration of IPA, a pair of counter-rotating attached vortices were observed to form to the side of the sphere and elliptical disks. These vortices appeared near the equator of the sphere. For the elliptical disks, the vortices appeared much further toward the wake in both orientations. These attached vortices were found to play a critical role in the stability of the straight-line motion of the surfers. A critical peak Reynolds number was found beyond which a transition from a straight-line translational motion to a rotational motion was observed for each surfer and surfer orientation. This rotational motion was only ever observed after the surfer had gone through a maximum in its velocity and had begun to decelerate. Two critical Reynolds number conditions were observed for the transition from a translational to rotational motion; a maximum Reynolds number achieved during the transient motion of the surfer and a Reynolds number during the deceleration phase at which the surfer begins to rotate. Just prior to rotation, the flow field was observed to become asymmetric and one of the vortices attached to the side of the sphere was observed to shed. The unbalanced torques resulting from vortex shedding destabilized the straight-line translational motion of the spherical Marangoni surfers and forced the spheres to rotate and begin to follow an orbital path.

For the sphere, a critical peak Reynolds number of $Re_{crit} = 285$ was found. At that flow rate, rotation was observed after the sphere decelerated to $Re = 90$. The sphere was found to be more stable than similarly sized circular disk-shaped Marangoni surfers which were found to have a critical peak Reynolds number of $Re_{crit} = 180$ [6]. This highlights the importance of surfer shape below the water line on stability. The stability of the elliptical disks were found to be strongly linked to their aspect ratio and their orientation. Independent of orientation, increasing the aspect ratio of the elliptical disk was found to make the disk more unstable. Additionally, at a given aspect ratio, elliptical disks traveling along their major axis where found to be more unstable than elliptical disks traveling along their minor axis or for that matter spheres or circular disks. Take, for example, an elliptical disk traveling along its major axis. For these surfers, a transition from straight-line motion to rotational motion was observed once a peak Reynolds number of $Re_{crit} = 180$ and $Re_{crit} = 120$ was obtained for aspect ratios of $AR = 1.5$ and $AR = 2$, respectively. The same surfers traveling along their minor axis were significantly more stable requiring a peak Reynolds number of $Re_{crit} = 330$ and $Re_{crit} = 240$ before rotation was observed. Thus, surfer geometry, symmetry, and orientation plays a large role on its stability.

The surfer geometry was also found to have a significant impact on the rotation rate. Increasing the aspect ratio of the elliptical disk was found to increase the rotation rate. Additionally, the rotation rate of the nonaxisymmetric elliptical disks was found to be more than an order of magnitude larger than the axisymmetric circular disks and spheres. It is clear from these observations, that breaking the surfer symmetry to produce a high aspect ratio elliptical disk designed to translate along its major axis would be an excellent approach toward designing high efficiency Marangoni propelled rotors, propellers, and mixers.

By allowing the spheres and the elliptical disks to interact with the edge of the Petri dish, the effects of the boundary and, in the case of the sphere, interface curvature were investigated. The presence of a rigid wall leads to an adverse pressure gradient necessary to bring the interfacial flow to rest. This adverse pressure gradient also decelerated the surfers as they approach the wall and can apply a torque to the sphere if they do not approach the wall along a perfectly radial flow trajectory. As a result, even on a flat interface, the presence of the boundary wall can cause the surfer to rotate. The major difference between the elliptical disks and the spheres is that the elliptical disks are neutrally buoyant and do not deform the interface around them. On the other hand, the spheres float below the interface resulting in a convex interfacial curvature around them. When the interface at the boundary of the Petri dish was flat, the repulsive force due to the mismatch in interface curvature around the sphere and near the boundary destabilized the sphere causing it to rotate at a maximum Reynolds number significantly lower, $Re_{crit} = 190$, than that observed for the unbounded case. Making the interface near the boundary concave increased this repulsive force further destabilizing the sphere, while making the interface convex resulted in an attractive force that fully stabilized the motion of the sphere at all Reynolds numbers tested.

For the case of an elliptical disk approaching the boundary of the Petri dish along a flat interface, the orientation of the surfer had a significant impact on its stability. For the elliptical disks traveling along its major axis, the presence of the boundary had little effect on its stability. The critical Reynolds number for rotation was statistically the same as the unbound case. However, for the elliptical disk traveling along its minor axis, the presence of the bounding wall was found to completely stabilize the motion of the surfer. Even at $100\,wt\%$ IPA and peak Reynolds numbers beyond $Re_{max} > 400$, no rotational motion was observed. This observation was quite different from the case of the axisymmetric spheres and circular disks [6] and suggests that surfer shape can be utilized to control the orientation and spatial arrangement of assemblies of Marangoni propelled surfers.

Funding Data

References

[1] Scriven, L. E., and Sternling, C. V., 1960, "The Marangoni Effects," Nature, **187**(4733), pp. 186–188.

[2] Rayleigh, L., 1889, "Measurements of the Amount of Oil Necessary in Order to Check the Motions of Camphor Upon Water," Proc. R. Soc. Lond., **47**, pp. 364–367.

[3] Suematsu, N. J., Ikura, Y., Nagayama, M., Kitahata, H., Kawagishi, N., Murakami, M., and Nakata, S., 2010, "Mode-Switching of the Self-Motion of a Camphor Boat Depending on the Diffusion Distance of Camphor Molecules," J. Phys. Chem. C, **114**(21), pp. 9876–9882.

[4] Renney, C., Brewer, A., and Mooibroek, T. J., 2013, "Easy Demonstration of the Marangoni Effect by Prolonged and Directional Motion: Soap Boat 2.0," J. Chem. Educ., **90**(10), pp. 1353–1357.

[5] Gidituri, H., Panchagnula, M. V., and Pototsky, A., 2019, "Dynamics of a Fully Wetted Marangoni Surfer at the Fluid–Fluid Interface," Soft Matter, **15**(10), pp. 2284–2291.

[6] Sur, S., Masoud, H., and Rothstein, J. P., 2019, "Translational and Rotational Motion of Disk-Shaped Marangoni Surfers," Phys. Fluids, **31**(10), p. 102101.

[7] Nakata, S., Iguchi, Y., Ose, S., Kuboyama, M., Ishii, T., and Yoshikawa, K., 1997, "Self-Rotation of a Camphor Scraping on Water: New Insight Into the Old Problem," Langmuir, **13**(16), pp. 4454–4458.

[8] Takabatake, F., Magome, N., Ichikawa, M., and Yoshikawa, K., 2011, "Spontaneous Mode-Selection in the Self-Propelled Motion of a Solid/Liquid Composite Driven by Interfacial Instability," J. Chem. Phys., **134**(11), p. 114704.

[9] Koyano, Y., Gryciuk, M., Skrobanska, P., Malecki, M., Sumino, Y., Kitahata, H., and Gorecki, J., 2017, "Relationship Between the Size of a Camphor-Driven Rotor and Its Angular Velocity," Phys. Rev. E, **96**(1), p. 012609.

[10] Nagai, K. H., Takabatake, F., Sumino, Y., Kitahata, H., Ichikawa, M., and Yoshinaga, N., 2013, "Rotational Motion of a Droplet Induced by Interfacial Tension," Phys. Rev. E, **87**(1), p. 013009.

[11] Angelini, T. E., Roper, M., Kolter, R., Weitz, D. A., and Brenner, M. P., 2009, "Bacillus subtilis Spreads by Surfing on Waves of Surfactant," PNAS, **106**(43), pp. 18109–18113.

[12] Fauvart, M., Phillips, P., Bachaspatimayum, D., Verstraeten, N., Fransaer, J., Michiels, J., and Vermant, J., 2012, "Surface Tension Gradient Control of Bacterial Swarming in Colonies of Pseudomonas aeruginosa," Soft Matter, **8**(1), pp. 70–76.

[13] Schildknecht, H., 1976, "Chemical Ecology-a Chapter of Modern Natural Products Chemistry," Angew. Chem. Int., **15**(4), pp. 214–222.

[14] Andersen, N. M., 1976, "A Comparative Study of Locomotion on the Water Surface in Semiaquatic Bugs (Insects, Hemiptera, Gerromorpha)," Vidensk. Meddr. Dan. Naturhist. Foren., **139**, pp. 337–396.

[15] Betz, O., 2002, "Performance and Adaptive Value of Tarsal Morphology in Rove Beetles of the Genus Stenus (Coleoptera, Staphylinidae)," J. Exp. Biol., **205**, pp. 1097–1113.

[16] Bush, J. W., and Hu, D. L., 2006, "Walking on water: Biolocomotion at the interface," Annu. Rev. Fluid Mech., **38**(1), pp. 339–369.

[17] Würger, A., 2014, "Thermally Driven Marangoni Surfers," J. Fluid Mech., **752**, pp. 589–601.

[18] Lauga, E., and Davis, A. M., 2012, "Viscous Marangoni Propulsion," J. Fluid Mech., **705**, pp. 120–133.

[19] Masoud, H., and Stone, H. A., 2014, "A Reciprocal Theorem for Marangoni Propulsion," J. Fluid Mech., **741**, pp. R41–R47.

[20] Masoud, H., and Shelley, M. J., 2014, "Collective Surfing of Chemically Active Particles," Phys. Rev. Lett., **112**(12), p. 128304.

[21] Vandadi, V., Kang, S. J., and Masoud, H., 2017, "Reverse Marangoni Surfing," J. Fluid Mech., **811**, pp. 612–621.

[22] Fei, W., Gu, Y., and Bishop, K. J., 2017, "Active Colloidal Particles at Fluid-Fluid Interfaces," Curr. Opin. Colloid Interface Sci., **32**, pp. 57–68.

[23] Vella, D., and Mahadevan, L., 2005, "The "Cheerios Effect," Am. J. Phys., **73**(9), pp. 817–825.

[24] Kralchevsky, P. A., and Nagayama, K., 2000, "Capillary Interactions Between Particles Bound to Interfaces, Liquid Films and Biomembranes," Adv. Coll. Int. Sci., **85**(2–3), pp. 145–192.

[25] Zeng, C., Bissig, H., and Dinsmore, A. D., 2006, "Particles on Droplets: From Fundamental Physics to Novel Materials," Solid State Commun., **139**(11–12), pp. 547–556.

[26] Daniello, R., Donnell, M., Khan, K., and Rothstein, J. P., 2014, "The Effect of Contact Angle and Density on the Orientation, Stability and Assembly of Floating Cubes," Phys. Rev. E, **89**(2), p. 023014.

[27] Kassuga, T. D., and Rothstein, J. P., 2015, "Buckling of Particle Laden Interfaces," J. Colloid Int. Sci., **448**, pp. 287–296.

[28] Kassuga, T. D., and Rothstein, J. P., 2016, "The Effect of Shear and Confinement on the Buckling of Particle-Laden Interfaces," J. Phys.: Condens. Matter, **28**(2), p. 025101.

[29] Cavallaro, M., Botto, L., Lewandowski, E. P., Wang, M., and Stebe, K. J., 2011, "Curvature-Driven Capillary Migration and Assembly of Rod-Like Particles," Proc. Natl. Acad. Sci., **108**(52), pp. 20923–20928.

[30] Loudet, J. C., and Pouligny, B., 2011, "How Do Mosquito Eggs Self-Assemble on the Water Surface?," Eur. Phys. J. E, **34**(8), p. 76.

[31] Sane, A., Mandre, S., and Kim, I., 2018, "Surface Tension of Flowing Soap Films," J. Fluid Mech., **841**, p. R2.

[32] White, F. M., 2003, Fluid Mechanics, McGraw-Hill, New York.

[33] Pimienta, V., and Antoine, C., 2014, "Self-Propulsion on Liquid Surfaces," Curr. Opin. Colloid Interface Sci., **19**(4), pp. 290–299.

[34] Zhang, L., Yuan, Y., Qiu, X., Zhang, T., Chen, Q., and Huang, X., 2017, "Marangoni Effect-Driven Motion of Miniature Robots and Generation of Electricity on Water," Langmuir, **33**(44), pp. 12609–12615.

[35] Morris, C. J., and Parviz, B. A., 2006, "Self-Assembly and Characterization of Marangoni Microfluidic Actuators," J. Micromech. Microeng., **16**(5), pp. 972–980.

[36] Varanakkottu, S. N., Anyfantakis, M., Morel, M., Rudiuk, S., and Baigl, D., 2016, "Light-Directed Particle Patterning by Evaporative Optical Marangoni Assembly," Nano Lett., **16**(1), pp. 644–650.

[37] Liu, I. B., Sharifi-Mood, N., and Stebe, K. J., 2016, "Curvature-Driven Assembly in Soft Matter," Philos. Trans. R. Soc. A: Math., Phys. Eng., **374**(2072), p. 20150133.